ADVANCED FUNCTIONAL MATERIALS
www.afm-journal.de

Wafer-Scale Growth of Aligned C_{60} Single Crystals via Solution-Phase Epitaxy for High-Performance Transistors

Zhengjun Lu, Wei Deng, Xiaochen Fang, Jie Xiao, Bei Lu, Xinwei Zhang, Azhar Ali Ayaz Pirzado, Jiansheng Jie, and Xiujuan Zhang**

Fullerene (C_{60}) single crystals with exceptionally low defects and nearly perfect translational symmetry make them appealing in achieving high-performance n-type organic transistors. However, because of its natural 0D structure, control over continuous crystallization of C_{60} over a large area is extremely challenging. Here, the authors report a solution-phase epitaxial approach for wafer-scale growth of continuously aligned C_{60} single crystals. This method enables the rational control of the density of nucleation event at meniscus front by confining the size and shape of meniscus with a microchannel template. In this case, a single nucleus as seed crystal can be formed at the front of meniscus, and then epitaxial growth from the seed crystal occurs with continuous retreat of the meniscus. As a result, highly uniform C_{60} single-crystal array with ultralow defect density is obtained on 2-inch substrate. Organic field-effect transistors made from the C_{60} single-crystal array show a high average electron mobility of 2.17 $cm^2 V^{-1} s^{-1}$, along with a maximum mobility of 5.09 $cm^2 V^{-1} s^{-1}$, which is much superior to the C_{60} polycrystalline film-based devices. This strategy opens new opportunities for the scalable fabrication of high-performance integrated devices based on organic crystals.

1. Introduction

Fullerene (C_{60}) and its derivatives with outstanding optoelectronic properties are identified to be promising materials to construct high-performance electronic and photonic devices, such as solar cells,[1–3] superconductors,[4,5] ferromagnets,[6] photodetectors,[7–9] tunnel transistors,[10] and organic field-effect transistors (OFETs),[11–14] owing to their highly conjugated molecular structures,[15] high electron-accepting,[16,17] and 3D electron-transporting properties.[18] Though most of the current applications rely on the use of C_{60} thin films, further improvement of the device performance is hindered by the intrinsic problems in the polycrystalline thin-film systems, such as abundant grain boundaries as well as a large number of defects.[19–22] Compared with the polycrystalline thin films, C_{60} single crystals with intrinsic lack of defects and grain boundaries possess superior optoelectronic properties in terms of higher carrier mobility and longer carrier diffusion length.[8] Many efforts have been devoted to growing high-quality C_{60} single crystals,[23–25] but sizes of the obtained C_{60} single crystals are usually very small (from several hundreds of nanometers to a few micrometers),[26] and the C_{60} crystals tend to form 0D morphologies owing to the naturally 0D structure of the C_{60} molecules.[27–30] To facilitate optoelectronic device applications, it is highly desirable to grow the C_{60} crystals with a continuous 1D or 2D (2D) architecture.

Up to now, several techniques, such as liquid/liquid interface precipitation (LLIP),[31–34] gel-assisted method,[8,23,35] and template-confined method,[36] have been developed to grow 1D or 2D C_{60} crystals. In the LLIP method, the good solvent/poor solvent interface created spatial confinements, and thus the crystallization of C_{60} molecules proceeded along the liquid/liquid interface, forming C_{60} nanorods or nanosheets.[34] The gel-assisted method relied on the gel as an inert matrix to suppress the isotropic crystallization originated from the naturally 0D structure of C_{60} and make 1D crystallization dominant.[23] Although these two methods enable the preparation of size-tunable C_{60} nanorods, nanosheets, and nanowires, the resultant crystals randomly dispersed in the solution, and it is difficult to transfer them to target substrates with ordered alignment. As a result, only discrete devices with very low integration levels

Z. J. Lu, W. Deng, X. C. Fang, B. Lu, X. W. Zhang, A. A. A. Pirzado, J. S. Jie, X. J. Zhang
Institute of Functional Nano & Soft Materials (FUNSOM), Jiangsu Key Laboratory for Carbon-Based Functional Materials & Devices
Soochow University
Suzhou, Jiangsu 215123, P. R. China
E-mail: dengwei@suda.edu.cn; xjzhang@suda.edu.cn
J. Xiao
School of Chemical and Environmental Engineering
College of Chemistry
Chemical Engineering and Materials Science
Soochow University
Suzhou, Jiangsu 215123, P. R. China
A. A. A. Pirzado
Department of Electronics Engineering
Faculty of Engineering and Technology
University of Sindh
Jamshoro, Sindh 76080, Pakistan
J. S. Jie
Macao Institute of Materials Science and Engineering
Macau University of Science and Technology
Taipa, Macau, SAR 999078, China

The ORCID identification number(s) for the author(s) of this article can be found under https://doi.org/10.1002/adfm.202105459.

DOI: 10.1002/adfm.202105459

could be achieved based on the C_{60} crystals. Also, the residual gel in the crystals is hard to be removed completely; either acid hydrolysis or heating treatment involved during the removal process may cause damage to the crystals. Recently, template-confined method had been demonstrated as an efficient strategy to directly grow 1D C_{60} crystal array on the desired substrates.[36] This method utilized the strongly space-confined effect of nanoscale channel templates to control 1D growth of C_{60} crystal array. And then the obtained 1D C_{60} crystal array could be transferred to substrate by a transfer printing process. However, the need for a complex transfer process and the small coverage area of the 1D C_{60} crystal array (<1 mm^2), due to the difficulty of uniform solution spreading in the nanoscale channels, impede its application for large-scale device fabrication.

Herein, we report for the first time a solution-phase epitaxial growth approach to achieve wafer-scale, highly aligned growth of uniform 1D C_{60} single-crystal array. In this method, microscale channels as a growth template have been used to confine the C_{60} solution and effectively reduce the size of the meniscus front, leading to the occurrence of a single nucleation event at the contact line. As a result, individual seed crystal will be formed at the contact position of meniscus front with the template, and the unidirectional motion of the meniscus causes continuously epitaxial growth of the seed crystals. This method enables highly aligned growth of 1D C_{60} single crystals with narrow diameter distribution and low defect density on 2-inch wafer. Significantly, OFETs made of the well-aligned and uniform C_{60} single crystals exhibit a high average electron mobility of 2.17 $cm^2\ V^{-1}\ s^{-1}$, along with a maximum mobility of 5.09 $cm^2\ V^{-1}\ s^{-1}$. The maximum mobility is ≈3.5 times compared to that of the state-of-the-art C_{60} polycrystalline film-based devices. Our work paves a new avenue for large-scale growth of high-quality C_{60} single crystals for organic electronics.

2. Results and Discussion

Figure 1a illustrates the solution-phase epitaxial growth method for large-scale growth of 1D C_{60} single-crystal array. A SiO_2 (300 nm)/Si wafer containing microscale photoresist (PR) channels was vertically inserted into the C_{60} solution (Figure 1a–i). The cross-sections of the channels present an inverted trapezoidal shape with a height of ≈1.4 µm (Figure S1, Supporting Information). The narrow channel produced a geometrical confinement effect, enabling the formation of concave meniscuses within the channels. Figure 1b shows the shape of the meniscus simulated by the computational fluid dynamics (see Discussion S1, Supporting Information, for the model details). The meniscus was restricted by the narrow and deep channel, resulting in a very tiny and thin solution tail at the top of the meniscus. In addition, the narrow meniscus forced the flow to compress, and thus enhanced convection flow, providing sufficient mass transport. This could significantly inhibit the dendritic growth of crystals that was commonly observed for organic crystals grown on flat substrate without

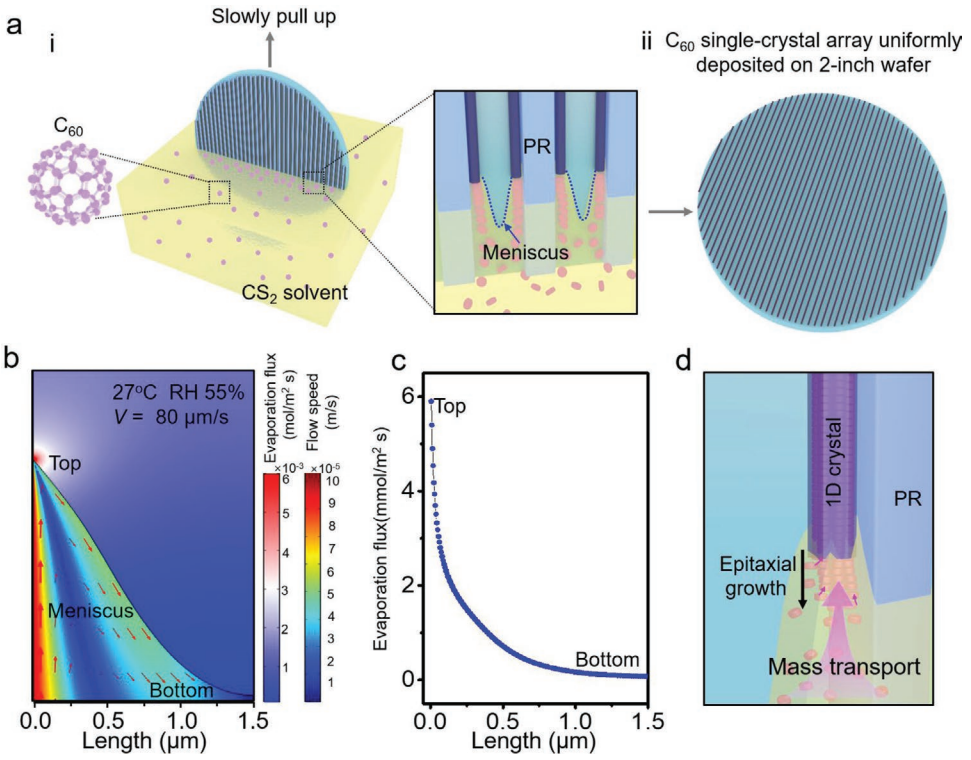

Figure 1. a) Schematic illustration of the solution-phase epitaxial process for wafer-scale growth of 1D C_{60} single-crystal array. The middle inset is a schematic illustration of the confined meniscus within the microscale PR channels. b) Multiphysics simulation results of the flow field in the liquid phase (meniscus) within the narrow channel and vapor flux in the air. c) Magnitude of evaporation flux of the solvent at the meniscus-air interface. d) Schematic illustration of the epitaxial growth process of a C_{60} single crystal.

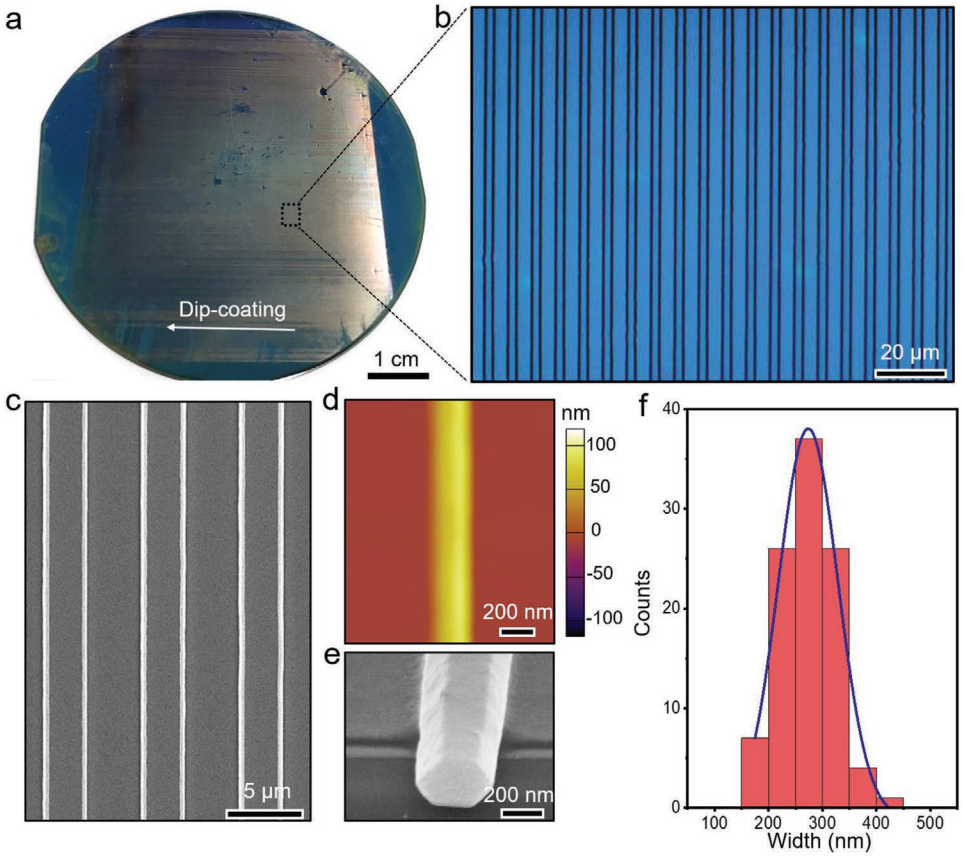

Figure 2. Morphology characterization of the wafer-scale 1D C_{60} single-crystal array. a) Photograph of the obtained 1D C_{60} crystal array on a BCB-covered 2-inch SiO_2/Si wafer. b) Representative OM image of the 1D C_{60} single-crystal array. c) Magnified SEM image of the 1D C_{60} single-crystal array. d) AFM image of a 1D C_{60} crystal, indicating that the crystal has a smooth surface. e) Cross-sectional SEM image of a crystal. f) Histogram of diameter distribution of the 1D C_{60} crystals.

the use of micro/nano-template (Figure S2, Supporting Information).[37–39] The distribution of the evaporation flux (J) at the liquid-air interface shows that the J at the top of the meniscus was 74 times greater than that at the bottom (Figure 1c), because of the large surface to volume ratio. As a result, a rapid nucleation would take place in the narrow region (i.e., meniscus front) where the density of nucleation events could be well controlled. In fact, this could lead to the formation of a single crystal nucleus, followed by a slow growth of high-quality C_{60} seed crystal at the meniscus front. As the wafer was slowly pulled out with an optimal speed of 80 μm s^{-1} (see Discussion S2 and Figure S3, Supporting Information for the detailed optimization process), upward flow would be triggered and the C_{60} molecules were transported to the pre-formed seed crystals (see arrows in meniscus in Figure 1b), leading to the appearance of C_{60} supersaturated phase. Then, C_{60} single crystals were formed along the sidewalls of PR channels through continuously epitaxial growth from the seed crystals (Figure 1d), hence we named this process as solution-phase epitaxial growth method. After removing the PR by acetone, wafer-scale 1D C_{60} single-crystal array could be obtained (Figure 1a (ii)). Besides the fluid dynamics, solvent is also critical for obtaining the high-quality C_{60} crystals. CS_2 is used as solvent in our method, since it has relatively low boiling temperature (46.2 °C) and surface tension (32.25 mN m^{-1}). The relatively low boiling temperature would bring a suitable evaporation rate, which facilitates the control on the crystallization velocity; and the low surface tension can produce a narrow meniscus front to reduce the nucleation densities. All these conditions are conductive to the uniform growth of crystals. Furthermore, CS_2 as a non-polar solvent cannot bring damage to the PR channel template.

Unlike previously reported template-confined method,[36] our solution-phase epitaxial growth approach is compatible with the high throughput, large-area solution coating method such as dip coating and blade coating, thus enabling the wafer-scale growth of 1D C_{60} crystals with an excellent uniformity. **Figure 2**a shows a photograph of the C_{60} single-crystal array that fabricated by the solution-phase epitaxial method using dip-coating approach on a divinyltetramethyldisiloxane bis(benzocyclobutene) (BCB)-covered 2-inch SiO_2/Si wafer. Optical microscopy (OM) images in Figure 2b and Figure S5, Supporting Information indicate that the unidirectional array is composed of a large number of parallel crystals. From the continuous shooting of the OM images along the growth direction of the C_{60} crystals in Figure S6, Supporting Information, it can be seen that the crystals uniformly covered on the 2-inch wafer with few ruptures. The zoomed-in scanning electron

microscope (SEM) image demonstrates that the intervals between C_{60} crystals precisely replicate the periodic structure of the PR stripes (Figure 2c). Atomic force microscope (AFM) image shows that the 1D crystal has a small surface roughness of about 1.5 nm r.m.s (Figure 2d). The cross-sectional SEM image in Figure 2e revealed that the prepared C_{60} crystal has a hexagonal end facet, implying the high crystal quality. Detailed SEM examination of hundreds of the C_{60} crystals indicates that the crystals have a narrow diameter distribution of 272.2 ± 48.5 nm (Figure 2f), thus the resultant C_{60} crystals can be defined as submicron wires. Note that the density and position of the C_{60} crystals could be readily controlled by tuning the widths or intervals of PR stripes, as shown in Figure S7a, Supporting Information. At relatively narrow spacing of 2, to 3, 5, and 10 μm, intervals between the adjacent C_{60} crystals can match well with the spacing of the PR stripes. Moreover, the resulting C_{60} crystals all have high quality with smooth surfaces and continuous structures. This ability to achieve highly aligned growth of C_{60} crystal array with controlled density is much desired for practical device applications. However, when the spacing was increased to 20 μm or more, discontinuous rod-like and even particle-like C_{60} crystals could be observed. At the wider spacing, the capillary force produced from the PR channels becomes weaker and meniscus would not be formed, as shown in Figure S7b, Supporting Information. In this case, "coffee-ring" effect would dominate, resulting in discontinuous crystallization.

The crystalline structure of the resulting C_{60} crystals was first examined by a powder X-ray diffraction (XRD). The corresponding powder XRD pattern in Figure S8, Supporting Information reveals a set of strong diffraction peaks of (00*l*) planes, which can be assigned to a CS_2-solvated monoclinic crystal structure.[14] The representative transmission electron microscope (TEM) image of the 1D C_{60} crystal in **Figure 3**a indicates that the crystal has clear edge and smooth surface. Selective-area electron diffraction (SAED) performed on different regions in one crystal or different crystals derived from the same substrate shows identical patterns with well-ordered diffraction spots (Figure S9, Supporting Information), manifesting the single-crystal nature of the crystals. Meanwhile, the growth direction can be determined to be [020] from the SAED patterns. High-resolution TEM (HRTEM) image collected along the short axis of crystal in Figure 3b reveals clear lattice fringes with a lattice spacing of 0.835 nm, which could be indexed as (200). According to the above results, {002} and {020} can be determined to be parallel and perpendicular to the long axis of crystal, and {200} is perpendicular to the short axis of crystal. Thus, it can be inferred that the side of the C_{60} crystal hexahedron is the {202} planes, as illustrated in Figure 3c. To examine the large-area structure homogeneity of the 1D C_{60} crystal array, grazing incidence X-ray diffraction (GIXRD) was performed using a synchrotron X-ray source with the X-ray irradiated region of 0.35×0.35 mm^2. The relatively large irradiated region guarantees that we can evaluate the crystallization quality of the C_{60} crystals at a larger scale. The C_{60} crystal array produces a series of distinct high-order spots in the direction of q_z (out of plane) and q_{xy} (in-plane) (Figure 3d), demonstrating that the C_{60} crystals within the X-ray irradiated region have a consistent crystallographic orientation. For comparison, GIXRD measurement on the thermally evaporated C_{60} thin film was also performed. The ring-like diffraction peaks manifest the polycrystalline structure of the thin film (Figure S10, Supporting Information). Besides, polarized optical microscope (POM) was used to assess the orientation and thickness variation of the C_{60} crystals in a large region through the observation of interference colors. POM image in Figure 3e shows consistent color of the 1D C_{60} crystal array, suggesting highly oriented crystalline structure as well as uniform thickness distribution of the C_{60} crystals. When the substrate was rotated relative to the polarizers' axes, the color change from bright to dark is homogenous across the 1D C_{60} crystal array (Figure 3f) and presents a fourfold symmetry (Figure 3g and Figure S11, Supporting Information). This is a clear indicator of the high crystal quality of the crystals. Further, the trap-state density (n_{traps}) in the C_{60} crystals was estimated from the current–voltage (*I*–*V*) curve following the standard space charge-limited current model.[40,41] An electron-only device with a channel length of about 200 μm was fabricated by connecting the 1D C_{60} single-crystal array between two LiF/Al electrodes. As shown in Figure 3h, the linear *I*–*V* section at low voltages represents an ohmic region (green). At the intermediate voltages, the current shows a steeply nonlinear rise (onset voltage, V_{TFL}) and signals the transition onto the trap-filled limit (TFL)-a regime in which all the available trap states are filled by the injected electrons.[42] The V_{TFL} is linearly proportional to the n_{traps}. As a result, n_{traps} of the C_{60} single-crystal array is estimated to be 1.62×10^{11} cm^{-3}, which is seven orders of magnitude lower than the evaporated C_{60} thin film (2×10^{18} cm^{-3}).[43] The above results collectively demonstrate that high-quality C_{60} single-crystal array is fabricated by the solution-phase epitaxial method.

Given the high uniformity and high crystal quality, the 1D C_{60} single-crystal array shows great potential for the application in large-scale organic electronics. We further fabricated top-contact bottom-gate OFETs based on the 1D C_{60} single-crystal array to evaluate their electrical properties (**Figure 4**a). A thin, thermally cross-linked BCB layer (150 nm) was coated over the surface of SiO_2 (300 nm)/Si substrate to eliminate electron traps that arise from hydroxyl groups.[44] Symmetric LiF (1.5 nm)/Al (200 nm) was deposited on the C_{60} single-crystal array as source (S) and drain (D) electrodes. Note that the LiF was adopted as an electron-injection layer at the contact interface to improve the charge injection efficiency. SEM image of a typical 1D C_{60} single-crystal array-based OFET in Figure 4b reveals a channel length (*L*) of 25 μm and an effective channel width (W_{eff}) of ≈11.4 μm by summing the width of all the C_{60} crystals in the channel, which covers ≈9.1% of the full OFET channel width. Cross-sectional SEM image of the Al/LiF/C_{60} array/BCB/SiO_2 stack in Figure 4c indicates that the 1D C_{60} single crystal is wrapped by the electrode and its bottom was fitted closely with the dielectric. Figures 4d,e show the transfer and electrical characteristics, respectively, of a representative 1D C_{60} single-crystal array-based OFET. The device exhibits typical n-channel OFET characteristics. Mobility of the OFET is estimated to be 2.82 cm^2 V^{-1} s^{-1} with a large on/off ratio (I_{on}/I_{off}) of ≈10^6 and a small leakage current of ≈10^{-12} A. More importantly, the device shows slight gate voltage (V_g) dependence, along with a high-reliability factor of 86% (Figure S12, Supporting Information),

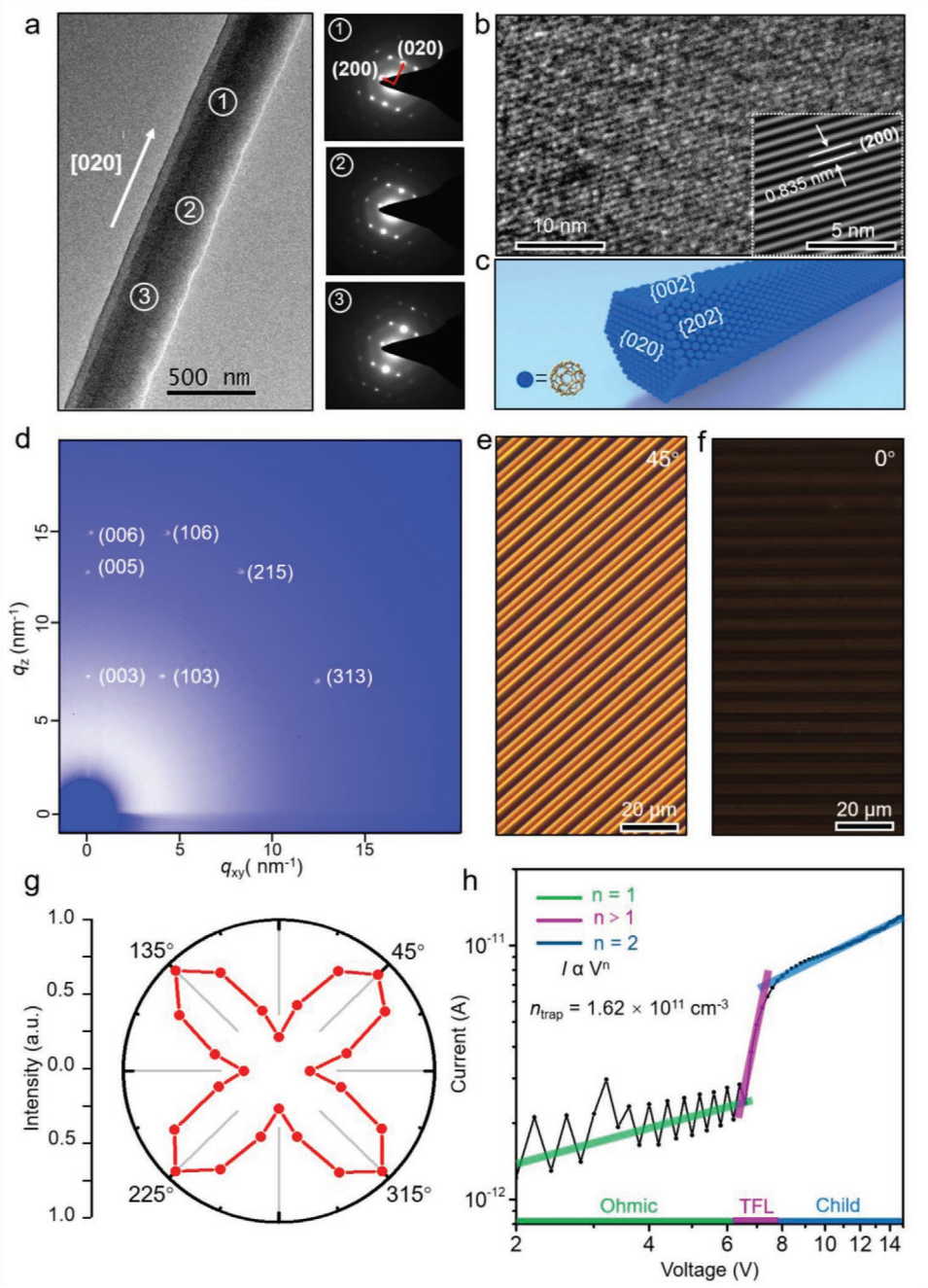

Figure 3. Crystal quality characterizations of the 1D C_{60} single-crystal array. a) TEM image of a 1D C_{60} single crystal (left) and corresponding SAED patterns recorded from the different marked positions (right). b) HRTEM image of a C_{60} crystal. c) Schematic diagram of the structure of the obtained 1D C_{60} single crystal. (d) GIXRD pattern of the 1D C_{60} single-crystal array. e,f) POM images of the 1D C_{60} single-crystal array acquired under different polarization angles of 45° and 0°, respectively. g) Angle-dependent polarized intensity of the 1D C_{60} single-crystal array. h) *I–V* trace of the 1D C_{60} single-crystal array.

which is superior to the C_{60} OFETs in previous reports[12–14] and suggests that the mobility value extracted from our devices is reliable. Meanwhile, the device shows a steep subthreshold slope of 2.3 V per decade and a near-zero V_{th} of 0.66 V. To the best of our knowledge, this V_{th} value is among the lowest for the OFETs based on C_{60} crystals, as depicted in Figure 4f. The small V_{th} manifests the low trap carrier density within the solution epitaxial C_{60} single-crystal array, which could be calculated using the following equation:[45]

$$V_{th} = V_{th,theoretical} + \frac{Q_t}{C_i} \quad (1)$$

where $V_{th,\ theoretical}$ is the theoretical V_{th}, Q_t is the trap carrier density in coulombs per square centimeter, and C_i is

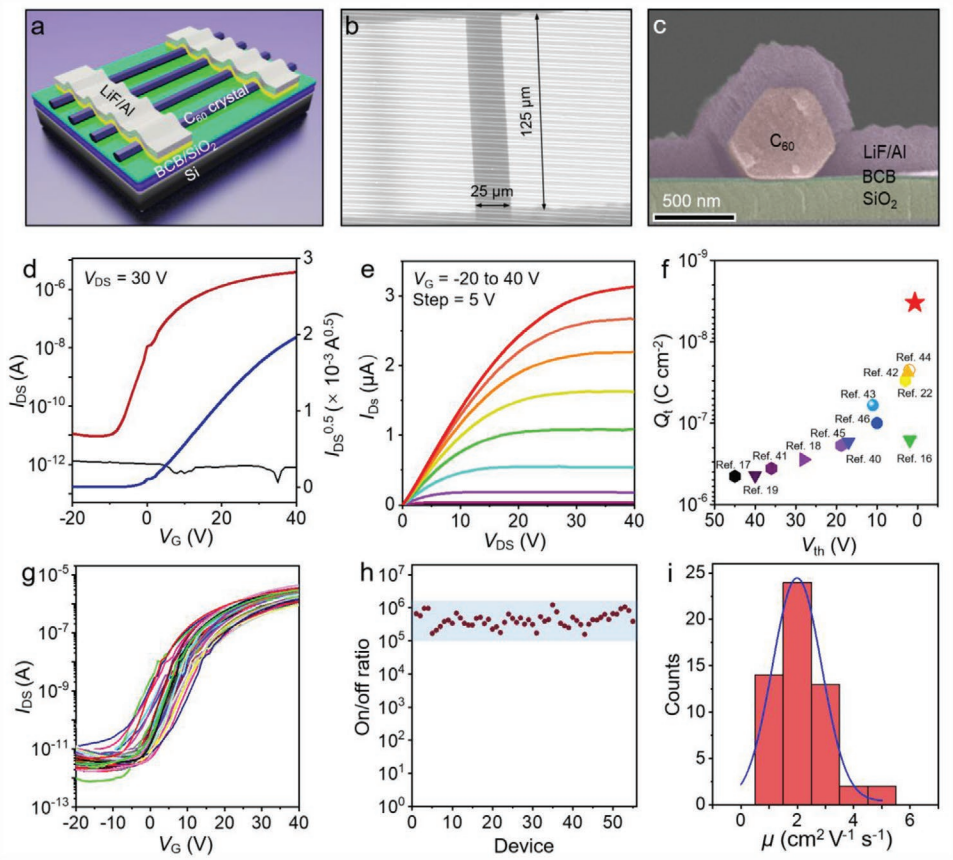

Figure 4. 1D C_{60} single-crystal array-based OFETs. a) Schematic illustration of the crystal array-based OFET and b) SEM image of a representative device. c) Cross-sectional SEM image of the OFET. d) Typical transfer and e) output characteristics of the OFET in the n-channel operation mode under a positive V_{DS} of 30 V. f) Trap carrier density comparison of the C_{60} crystals prepared with different methods. g) Transfer curves of 55 C_{60} single-crystal array-based OFETs on the same substrate. h) I_{on}/I_{off} ratio distribution and i) mobility histogram of the 55 OFETs.

the capacitance/area of the gate dielectric. In this way, the trap carrier density of the 1D C_{60} crystal array is estimated to be as low as 3.31×10^{-9} C cm^{-2}, which is 7–136 times lower than that of the C_{60} crystals prepared by previously reported methods (Figure 4f and Table S1, Supporting Information).[11–14,20,46–52] The excellent device performance of the OFET device could be attributed to the high crystal quality of 1D C_{60} single crystal and the optimized device structure with good electrical contacts. Next, the performance uniformity of 55 C_{60} crystal array-based devices on the same substrate was investigated. Figure 4g depicts a plot of overlaid transfer curves of the 55 OFETs measured at the same condition. It is observed that all the devices exhibit typical n-channel transfer characteristics with similar I_{on}/I_{off} ratio of 10^5–10^6 (Figure 4h) and ideal linear characteristics with high average reliability of 78.4% (Figure S13, Supporting Information). The good device-to-device uniformity is ascribed to the uniform sizes and structures as well as the well-ordered alignment of the C_{60} crystals. The average mobility of our devices is 2.17 ± 0.93 cm^2 V^{-1} s^{-1} (histogram in Figure 4i). Notably, the maximum mobility is as high as 5.09 cm^2 V^{-1} s^{-1} for the C_{60} single-crystal array-based OFETs, which is at least 3.5 times higher than that of the OFETs based on the previously reported C_{60} polycrystalline films (Table S2, Supporting Information).[20–22,46,49–52] Finally, the air stability of the C_{60} single-crystal array-based OFET was examined. As shown in Figure S14, Supporting Information, the mobility value of the OFET decreased ≈40% after 1-day exposure in air, which is comparable to the air stability of the reported C_{60} polycrystalline films.[53] The ambient instability of C_{60} single crystal-based device is due to low electron affinity of C_{60} molecules and can be improved through device encapsulation.[54]

3. Conclusion

In conclusion, we presented a solution-phase epitaxial approach to achieve wafer-scale growth of the 1D C_{60} single-crystal array. By using PR microchannels as template, both sizes of and shapes of the meniscus fronts in the solution growth process could be rationally controlled, enabling the formation of individual seed crystal at each meniscus front. With the unidirectional motion of the meniscus, C_{60} molecules were then continuously transported to the meniscus fronts, thereby causing epitaxial growth of the seed crystals. The resultant 1D C_{60} single crystals had uniform morphology and structure, revealing a defect density as low as 1.62×10^{11} cm^{-3}. As a result, 55 OFETs made from the C_{60} crystal

array on the same substrate exhibited a high average electron mobility of 2.17 $cm^2 V^{-1} s^{-1}$, and the maximum mobility of 5.09 $cm^2 V^{-1} s^{-1}$ is ≈3.5 times of that for the state-of-the-art C_{60} polycrystalline films. This work establishes a simple yet efficient approach for the fabrication of large-area C_{60} single crystals, facilitating the development of high-performance organic integrated devices.

4. Experimental Section

Materials: C_{60} was purchased from Sigma-Aldrich and used without further purification. C_{60} solution was prepared by dissolving 5 mg C_{60} powder in CS_2 solvent (10 mL, HPLC). BCB (Cyclotene, 3022-35) was purchased from Dow Chemicals. All materials were used as received.

Fabrication of Microscale PR Channels: Microscale PR channels were prepared by following steps. First, BCB solution was spin-coated on the clean SiO_2 (300 nm)/Si wafer at 2000 rpm for 45 s and then prebaked at 160 °C for 30 min and annealed at 260 °C for 2 h, yielding 150 nm BCB layer on the wafer. Second, positive PR (Allresist, AR-P5350) was spin-coated on the BCB-covered wafer at 2000 rpm for 45 s and then annealed at 100 °C for 3 min. Then, the wafer was exposed by UV light through a patterned mask to the PR. After that, the exposed portions of the PR were dissolved by a chemical developer (Allresist, AR300-26). Finally, periodic strips of PR with a gap of 3 μm were generated on the BCB-covered wafer, forming microscale PR channels.

Growth of 1D C_{60} Single-Crystal Array: In a typical growth process, the microscale PR channels as template were immersed in the C_{60}/CS_2 solution at room temperature, and then, the substrate was pulled up by a stepped-motor at a steady speed of 80 μm s^{-1}. After that, the sample was immersed in acetone for 2 s to remove the PR, and then dried with a stream of nitrogen to obtain 1D C_{60} single-crystal array.

Characterization of C_{60} Single Crystals: Morphologies of the aligned C_{60} crystal array were characterized using cross-polarized OM (Leica, DMDM4000M), SEM (Carl Zeiss, Supra 55), and AFM (Oxford, Asylum Cypher S). TEM (FEI, Tecnai G2 F20) was used to characterize the crystal quality of the C_{60} crystals. GIXRD measurements were performed on the BL14B1 beamline (energy = 10 keV) at the Shanghai Synchrotron Radiation Facility. The distance from the sample to detector was 340 mm, and the diffraction patterns were acquired for 90 s with a 2D charge-coupled device (2DCCD) detector.

Device Fabrication and Measurements: Top-contact, bottom-gate OFETs were fabricated by thermally evaporating 1.5 nm LiF and 200 nm Al films as a source and drain electrodes on the obtained C_{60} single-crystal array. The OFET channel length and width were 25 and 125 μm, respectively, which were defined by the shadow mask. The effective device channel width was calculated by summing the width of all the C_{60} crystals in the channel. The C_i of the BCB/SiO_2 dielectric was measured to be 5.02 nF cm^{-2} (Figure S15, Supporting Information). All the devices were characterized by a semiconductor characterization system (Keithley SCS-4200) on a probe state in an N_2-filled glove box.

Supporting Information

Supporting Information is available from the Wiley Online Library or from the author.

Acknowledgements

This work was supported by the National Natural Science Foundation of China (Grant Nos. 51973147, 61904117, and 51821002), the Natural Science Foundation of Jiangsu Province of China (No. BK20180845), the Priority Academic Program Development of Jiangsu Higher Education Institutions (PAPD), and Collaborative Innovation Center of Suzhou Nano Science and Technology (Nano-CIC). They also thank the beamlines BL14B1 (Shanghai Synchrotron Radiation Facility) for providing the beamtime.

Conflict of Interest

The authors declare no conflict of interest.

Data Availability Statement

The data that supports the findings of this study are available in the supplementary material of this article.

Keywords

aligned structures, C_{60} single crystals, large-area growth, organic field-effect transistors, solution-phase epitaxy

Received: June 7, 2021
Revised: July 26, 2021
Published online:

[1] S. Ullbrich, J. Benduhn, X. K. Jia, V. C. Nikolis, K. Tvingstedt, F. Piersimoni, S. Roland, Y. Liu, J. Wu, A. Fischer, D. Neher, S. Reineke, D. Spoltore, K. Vandewal, *Nat. Mater.* **2019**, *18*, 459.
[2] T. Gattia, E. Mennaa, M. Meneghettia, M. Magginia, A. Petrozzab, F. Lambertia, *Nano Energy* **2017**, *41*, 84.
[3] H. Li, K. Lu, Z. Wei, *Adv. Energy Mater.* **2017**, *7*, 1602540.
[4] S. -Z. Wang, M. -Q. Ren, S. Han, F. -J. Cheng, X. -C. Ma, Q. -K. Xue, C. -L. Song, *Commun. Phys.* **2021**, *4*, 114.
[5] Ś. Chakravarty, S. A. Kivelson, M. I. Salkola, S. Tewari, *Science* **1992**, *256*, 1306.
[6] P.-M. Allemand, K. C. Khemani, A. Koch, F. Wudl, K. Holczer, S. Donovan, G. Grüner, J. D. Thompson, *Science* **1991**, *253*, 301.
[7] J. Ren, M. Niu, X. Guo, Y. Liu, X. Yang, M. Chen, X. Hao, Y. Zhu, H. Chen, H. Li, *J. Am. Chem. Soc.* **2020**, *142*, 1630.
[8] K. Liu, S. Gao, Z. Zheng, X. Deng, S. Mukherjee, S. Wang, H. Xu, J. Wang, J. Liu, T. Zhai, Y. Fang, *Adv. Mater.* **2019**, *31*, 1808254.
[9] R. Saran, R. J. Curry, *Small* **2018**, *14*, 1703624.
[10] A. Guo, Y. Fu, L. Guan, J. Liu, Z. Shi, Z. Gu, R. Huang, X. Zhang, *Nanotechnology* **2006**, *17*, 2655.
[11] P. Kumar, Y. Gerchikov, K. N. Shivananda, A. Sadeh, Y. Eichen, N. Tessler, *Adv. Electron. Mater.* **2016**, *2*, 1500309.
[12] T. H. Lee, K. Kim, G. Kim, H. J. Park, D. Scullion, L. Shaw, M.-G. Kim, X. Gu, W.-G. Bae, E. J. G. Santos, Z. Lee, H. S. Shin, Y. Nishi, Z. Bao, *Chem. Mater.* **2017**, *29*, 2341.
[13] H. Li, B. C-K. Tee, J. J. Cha, Y. Cui, J. W. Chung, S. Y. Lee, Z. Bao, *J. Am. Chem. Soc.* **2012**, *134*, 2760.
[14] K. -Y. Wu, T. -Y. Wu, S. -T. Chang, C. -S. Hsu, C. -L. Wang, *Adv. Mater.* **2015**, *27*, 4371.
[15] Y. Hashikawa, T. Fushino, Y. Murata, *J. Am. Chem. Soc.* **2020**, *142*, 20572.
[16] M. Chen, R. Guan, S. Yang, *Adv. Sci.* **2019**, *6*, 1800941.
[17] A. R. P. Santiago, O. Fernandez-Delgado, A. Gomez, M. A. Ahsan, L. Echegoyen, *Angew. Chem., Int. Ed.* **2021**, *60*, 122.
[18] Q. Burlingame, C. Coburn, X. Z. Che, A. Panda, Y. Qu, S. R. Forrest, *Nature* **2018**, *554*, 77.

[19] H. H. Choi, A. F. Paterson, M. A. Fusella, J. Panidi, O. Solomeshch, N. Tessler, M. Heeney, K. Cho, T. D. Anthopoulos, B. P. Rand, V. Podzorov, *Adv. Funct. Mater.* **2019**, *29*, 1903617.
[20] Y. J. Jeong, D.-J. Yun, J. Jang, S. Park, T. K. An, L. H. Kim, S. H. Kim, C. E. Park, *Phys. Chem. Chem. Phys.* **2015**, *17*, 6635.
[21] M. Irimia-Vladu, N. Marjanovic, A. Vlad, A. M. Ramil, G. Hernandez-Sosa, R. Schwödiauer, S. Bauer, N. S. Sariciftci, *Adv. Mater.* **2008**, *20*, 3887.
[22] T. D. Anthopoulos, B. Singh, N. Marjanovic, N. S. Sariciftci, A. M. Ramil, H. Sitter, M. Cölle, D. M. de Leeuw, *Appl. Phys. Lett.* **2006**, *89*, 213504.
[23] V. S. Nair, R. D. Mukhopadhyay, A. Saeki, S. Seki, A. Ajayaghosh, *Sci. Adv.* **2016**, *2*, e1600142.
[24] K. Lee, B. Choi, I. J.-L. Plante, M. V. Paley, X. Zhong, A. C. Crowther, J. S. Owen, X. Zhu, X. Roy, *Angew. Chem., Int. Ed.* **2018**, *57*, 6125.
[25] J. Kim, C. Park, I. Song, M. Lee, H. Kim, H. C. Choi, *Sci. Rep.* **2016**, *6*, 32205.
[26] A. L. Briseno, S. C. B. Mannsfeld, M. M. Ling, S. Liu, R. J. Tseng, C. Reese, M. E. Roberts, Y. Yang, F. Wudl, Z. Bao, *Nature* **2006**, *444*, 913.
[27] E. Nakamura, H. Isobe, *Acc. Chem. Res.* **2003**, *36*, 807.
[28] T. Nakanishi, W. Schmitt, T. Michinobu, D. G. Kurthac, K. Ariga, *Chem. Commun.* **2005**, *48*, 5982.
[29] S. S. Babu, H. Möhwaldb, T. Nakanishi, *Chem. Soc. Rev.* **2010**, *39*, 4021.
[30] T. Michinobu, T. Nakanishi, J. P. Hill, M. Funahashi, K. Ariga, *J. Am. Chem. Soc.* **2006**, *128*, 10384.
[31] H. R. Barzegar, F. Nitze, A. Malolepszy, L. Stobinski, C. -W. Tai, T. Wågberg, *Molecules* **2012**, *17*, 6840.
[32] H. -X. Ji, J. -S. Hu, Q. -X. Tang, W. -G. Song, C. -R. Wang, W. -P. Hu, L. -J. Wan, S. -T. Lee, *J. Phys. Chem. C* **2007**, *111*, 10498.
[33] K. Ogawa, T. Kato, A. Ikegami, H. Tsuji, N. Aoki, Y. Ochiaia, *Appl. Phys. Lett.* **2006**, *88*, 112109.
[34] M. Sathish, K. Miyazawa, *J. Am. Chem. Soc.* **2007**, *129*, 13816.
[35] C. Zhang, J. Wang, J. -J. Wang, M. Li, X. -L. Yang, H. -B. Xu, *Chem. - Eur. J.* **2012**, *18*, 14954.
[36] K. S. Park, B. Cho, J. Baek, J. K. Hwang, H. Lee, M. M. Sung, *Adv. Funct. Mater.* **2013**, *23*, 4776.
[37] R. Janneck, F. Vercesi, P. Heremans, J. Genoe, C. Rolin, *Adv. Mater.* **2016**, *28*, 8007.
[38] W. Deng, X. Zhang, H. Dong, J. Jie, X. Xu, J. Liu, L. He, L. Xu, W. Hu, X. Zhang, *Mater. Today* **2019**, *24*, 17.
[39] Z. Zhang, B. Peng, X. Ji, K. Pei, P. K. L. Chan, *Adv. Funct. Mater.* **2017**, *27*, 1703443.
[40] J. Dacuna, A. Salleo, *Phys. Rev. B* **2011**, *84*, 195209.
[41] R. W. I. de Boer, M. Jochemsen, T. M. Klapwijk, A. F. Morpurgo, J. Niemax, A. K. Tripathi, J. Pflaum, *J. Appl. Phys.* **2004**, *95*, 1196.
[42] W. Deng, J. Jie, X. Xu, Y. Xiao, B. Lu, X. Zhang, X. Zhang, *Adv. Mater.* **2020**, *32*, 1908340.
[43] W. L. Kalb, S. Haas, C. Krellner, T. Mathis, B. Batlogg, *Phys. Rev. B* **2010**, *81*, 155315.
[44] W. Deng, Y. L. Xiao, B. Lu, L. Zhang, Y. J. Xia, C. H. Zhu, X. J. Zhang, J. H. Guo, X. H. Zhang, J. S. Jie, *Adv. Mater.* **2021**, *33*, 2005915.
[45] C. Jiang, H. W. Choi, X. Cheng, H. Ma, D. Hasko, A. Nathan, *Science* **2019**, *363*, 719.
[46] S. Kobayashi, T. Takenobu, S. Mori, A. Fujiwara, Y. Iwasa, *Sci. Technol. Adv. Mater.* **2003**, *4*, 371.
[47] H. Li, C. Fan, M. Vosgueritchian, B. C.-K. Teec, H. Chen, *J. Mater. Chem. C* **2014**, *2*, 3617.
[48] W. Kang, M. Kitamura, T. Itoh, Y. Arakawa, *Jpn. J. Appl. Phys.* **2012**, *51*, 11PD06.
[49] C.-F. Sung, D. Kekuda, L. F. Chu, Y.-Z. Lee, F.-C. Chen, M.-C. Wu, C. -W. Chu, *Adv. Mater.* **2009**, *21*, 4845.
[50] M. Kitamura, Y. Kuzumoto, M. Kamura, S. Aomori, Y. Arakawa, *Appl. Phys. Lett.* **2007**, *91*, 183514.
[51] M. Chikamatsu, S. Nagamatsu, T. Taima, Y. Yoshida, N. Sakai, H. Yokokawa, K. Saito, K. Yase, *Appl. Phys. Lett.* **2004**, *85*, 2396.
[52] T. Kanbara, K. Shibata, S. Fujiki, Y. Kubozono, S. Kashino, T. Urisu, M. Sakai, A. Fujiwara, R. Kumashiro, K. Tanigaki, *Chem. Phys. Lett.* **2003**, *379*, 223.
[53] R. Ahmed, M. Sams, C. Simbrunner, M. Ullah, K. Rehman, G. Schwabegger, H. Sitter, T. Ostermann, *Synth. Met.* **2012**, *161*, 2562.
[54] V. V. Aksenova, R. M. Nikonova, V. I. Lad'yanov, N. B. Tamm, E. V. Skokan, B. E. Pushkarev, *Russ. J. Phys. Chem.* **2013**, *87*, 1749.